




## Article

# Statistics and 3D Modelling on Soil Analysis by Using Unmanned Aircraft Systems and Laboratory Data for a Low-Cost Precision Agriculture Approach

Alessandro Mei <sup>1,\*</sup> , Alfonso Valerio Ragazzo <sup>1,2</sup>, Elena Rantica <sup>1</sup> and Giuliano Fontinovo <sup>1</sup>

<sup>1</sup> Institute of Atmospheric Pollution Research, National Research Council (CNR), Area della Ricerca Roma 1, Strada Provinciale 35d, 9, Montelibretti, 00010 Rome, Italy; alfonsovalerioragazzo@cnr.it (A.V.R.)

<sup>2</sup> Unit of Electronics for Sensor Systems, Department of Science and Technology for Sustainable Development and One Health, Campus Bio-Medico University of Rome, Via Alvaro del Portillo 21, 00128 Rome, Italy

\* Correspondence: alessandro.mei@cnr.it

**Abstract:** The aim of this work was to elaborate a new methodology that can allow for the identification of the topsoil homogeneous area (tSHA) distribution along land parcels, supporting farmers in keeping low-cost, sustainable, and light logistic management of precision agriculture (PA) practices. This paper shows the assessment of tSHA variability over two production units (PUs), considering radiometric response (optical camera), physicochemical (texture, pH, electrical conductivity), and statistical and geostatistical data analysis. By using unmanned aircraft systems (UASs) and laboratory analysis, our results revealed that the integration between UAS-RGB and physicochemical data can improve the estimation accuracy of tSHA distribution. Firstly, the UAS-RGB dataset was used to isolate bare soil from the vegetative radiometric contribution. Secondly, starting from statistical approaches (correlation matrices), the highest correlation with UAS-RGB and physicochemical data was stated. Thirdly, by using a geostatistical approach (ordinary cokriging), the map representing the tSHA variability was finally obtained.

**Keywords:** remote sensing; UAS; soil texture; precision agriculture; statistics



**Citation:** Mei, A.; Ragazzo, A.V.; Rantica, E.; Fontinovo, G. Statistics and 3D Modelling on Soil Analysis by Using Unmanned Aircraft Systems and Laboratory Data for a Low-Cost Precision Agriculture Approach. *AgriEngineering* **2023**, *5*, 1448–1468. <https://doi.org/10.3390/agriengineering5030090>

Academic Editors: Jing Zhou, Lirong Xiang and Lin Wei

Received: 18 April 2023

Revised: 11 August 2023

Accepted: 23 August 2023

Published: 30 August 2023



**Copyright:** © 2023 by the authors. Licensee MDPI, Basel, Switzerland. This article is an open access article distributed under the terms and conditions of the Creative Commons Attribution (CC BY) license (<https://creativecommons.org/licenses/by/4.0/>).

## 1. Introduction

Due to the demand increase in world's food supply over the last thirty years, food production has had considerable growth, reflected in the improvement of expanded irrigation and fertilization/pesticides use [1]. In the agri-food production chain, precision agriculture (PA) practices are now required to allow the increase in knowledge about spatial distribution of homogeneous soil areas within land parcels and the supply of innovative approaches for resource and practice management in agricultural contexts [2,3]. As well as on PA, this paper is focused on a new procedure for soil surface variability retrieval, being the result of complex relations between biological (e.g., pests and microbes), geological (e.g., geochemical setting of the substrate and parent material), pedological (e.g., soil horizons distribution, lisciviation processes, texture, and available water capacity), edaphic (e.g., salinity, nutrients, organic matter, and humification processes), agronomic (e.g., agricultural practices, choice of rootstock, pre-planting, and cultivation management), climatic (e.g., temperature, rainfall, and humidity), topographic (e.g., slope, elevation, and exposition), and anthropogenic factors.

Site-specific soil analysis can facilitate crop supervision on pre-planting and post-planting sceneries by considering physicochemical local variability [4,5]. To understand the soil-crop system, it is necessary to consider soil property effects for a given culture, first through preliminary/non-invasive analysis and, consequently, through specific/invasive investigations. According to this, preliminary/non-invasive measurements can provide information by detecting soil texture, electrical conductivity (EC), pH, and remote sensing

spectral response [5–8]. Conversely, specific/invasive techniques concern a pedological survey along the soil profile ( $\approx 2$  m-depth), followed by dry/wet-chemistry laboratory analysis for each diagnostic soil horizon [5,9,10]. Concerning preliminary and non-invasive methods, the utilization of remote sensing (e.g., satellite and UAS) imagery can make available the obtaining of information on topsoil homogeneous area (tSHA) distribution in relation to the physicochemical variability. For instance, tSHA detection can arise through a combination of optical sensors with electrical, acoustic, and electrochemical capabilities [11]. Furthermore, through statistical predictive models, many authors used visible and/or near-infrared spectroscopy to determine textural classes or soil organic matter (SOM) contents [12,13]. De facto, in recent years, PA has increasingly seen a spread about the specific use of unmanned aircraft systems (UASs) and satellites for the study of plant condition [14–17] and soil characteristics [18–22]. According to this, to feature homogeneous areas on bare soil, pixel reflectance can be coupled with soil parameters and values related to remote datasets (satellite and UAS) [23–25].

Nowadays, the use of UAS in agricultural applications is rising considerably, and the constant demand of such kinds of tools is producing a significant economic influence [26]. Hence, such tendencies appear in the augmentation of research papers on the application of sensors set on unmanned aircraft vectors (UAVs), especially in the PA context [27–32]. Such a trend is mainly supported by six principal factors: (i) camera and sensor equipment is still low cost; (ii) easy application and employment of sensors and cameras on vectors; (iii) non-destructive measures; (iv) effectiveness to recover the canopy volume and pedological property; (v) utilization of structure from motion (SfM) techniques by computer vision approach; and (vi) development of automatic-feature-matching algorithms [23–37].

Datasets retrieved from UAS, through the combination of 2D/3D data analysis, are also used for map degradation processes in vineyards, providing essential information for replanting or redeveloping procedures; matching the canopy volume with soil properties; and pointing out parameters such as cultivar vigor, yields, irrigation design, canopy volume, leaf area, plant height, vine row extraction, and yield estimation [38–41]. Hence, the latest advances are showing an intensive growth of works related to dense point cloud acquisition, extraction of traits derived from digital elevation models (DEMs), and 3D model computations. According to this, to visualize morphometric features, UAS-RGB data elaboration and map algebra operations from digital surface models (DSMs) and digital terrain models (DTMs) can be used to obtain products such as digital difference models (DDMs) [42,43]. Then, in PA contexts, soil characteristics retrieval can occur through satellite, UAS, and laboratory analysis, obtaining spectral indices and predicting pedological parameters such as the soil texture. Such a kind of analysis can be helpful for better initial growth during the pre-planting stage, aiming to organize agricultural practices. As well as in this paper, superficial soil radiometric parameters can be useful for a preliminary discrimination of tSHAs along land parcels, retrieving information on their spatial distribution. Then, such datasets are related to the distribution of areas potentially affected by anomalies and lack. As performed in this paper, topsoil heterogeneity, which could be related to anomalies and nutrient deficiencies, can be spatialized through the proposed procedure by using UAS-RGB imagery and topsoil physicochemical parameters' estimation. Then, the data are analyzed with the aim of obtaining a functional spatialization in relation to the UAS-RGB technology image acquisition. According to this, the dataset used in this work concerns results and evaluations obtained through the following activities:

- (i) Ground sample campaign and laboratory analysis (EC, pH, and soil texture);
- (ii) UAS-RGB survey and spectral indices' calculation;
- (iii) Statistics and geostatistics.

## 2. Materials and Methods

### 2.1. Study Area and Geopedological Setting

The area of interest lies within the region of Calabria (Italy), in the municipal area of Gerace, in the central-eastern part of the Reggio Calabria Province, between Novito and Gerace streams, within a territory named Locride, at an altitude of 492 MASL (Figure 1). Regarding the study area, it is situated between the mountain ranges of Serre and Aspermont, exactly on the southeastern segment of the Calabrian Apennine. Several production units (PUs) are located at about 200 MASL, in a north/south region sheltered from sea winds by east crests: Greco Bianco and the Greco Nero types of grapevines are present. Referring to Csa class from the Koppen classification, climate condition concerns a hot summer Mediterranean climate with hot and dry summers and moderately temperate winters [44]. The yearly means of temperature, evapotranspiration, and precipitation are 18.4 °C, 87.3 mm, and 61.2 mm, respectively.

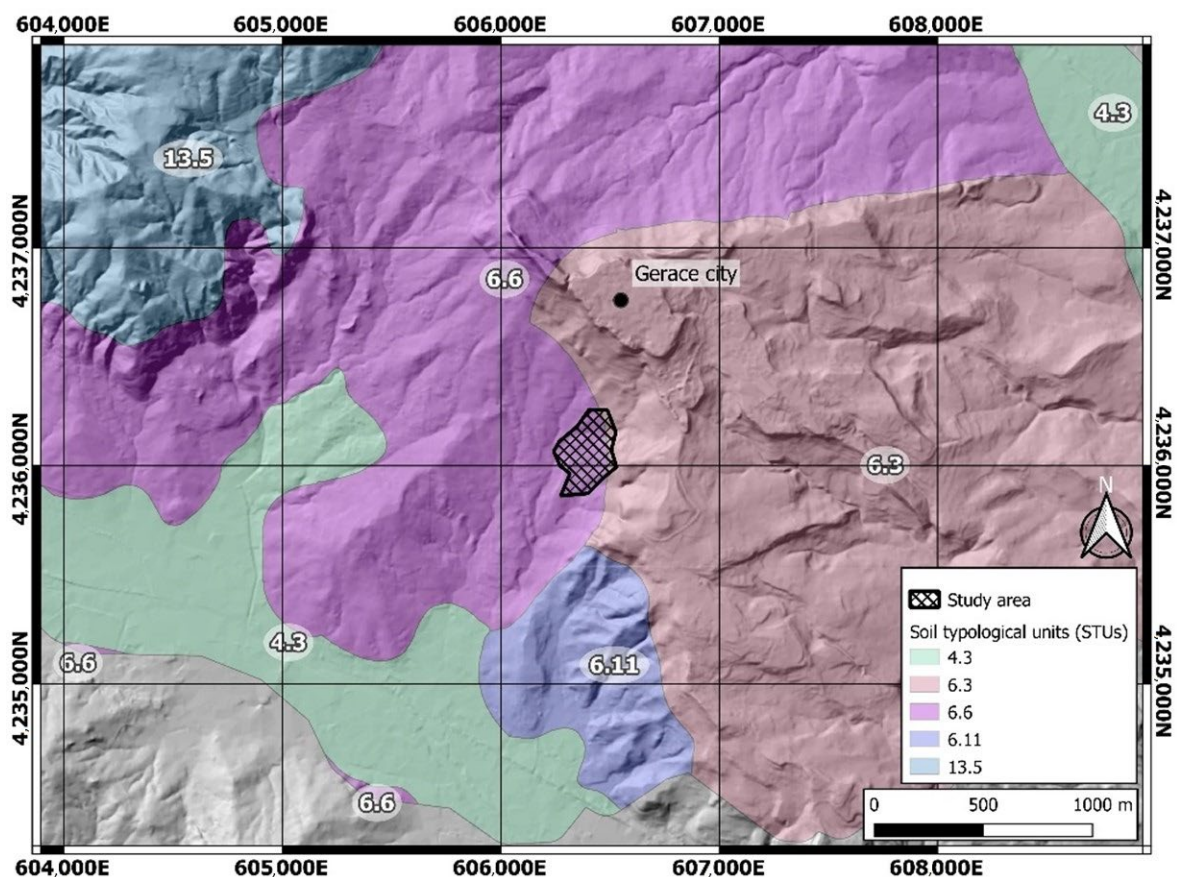


**Figure 1.** This image represents the study area and the spatialization of the soil cartographic units with their relative STUs (6.3 and 6.6).

The Calabrian geological setting derives from the tectonic structuring that occurred with the continuous north-westward subduction of the Ionian oceanic lithosphere underneath the Calabrian–Peloritani arc [44–46] and the south-eastward roll-back of the Ionian slab [47]. According to Sheet CARG 590 [48], the geological formations are related to sedimentary lithotypes. These are denoted by (i) the Apennine–Maghrebide Orogenetic Unit (Argille Variegata AV-Group), (ii) the Terrigenous Miocene Succession (Pier Niceto Formation-PCT), and (iii) the Clastic-Evaporitic Messinian Succession (Vincio's Calcarenitone-VNI). More precisely, the AV-Group belongs to a deep basin depositional environment (Upper Cretaceous–Lower Miocene), the PCT-Formation (Serravallian–Tortonian) belongs both to the continental slope and the base of slope, and the VNI from pelitic to shallow marine calcarenite formations [49,50]. Thus, the previous formations are characterized

by the subsequent lithotypes, respectively: pelite (quartzarenite and limestone); marine pre-evaporitic pelite (limestone–gypsum); coarse-grained alluvial-fan to conglomerates; and sandy shallow-marine to continental progradation lithotype [48–50]. According to the previous geological classification, the substrate can influence the composition of the soils above through pedogenetic processes. Hence, in the area of interest, tSHAs can inherit their chemical and physical properties from the geological context. For instance, textural properties, such as the abundance of sand, confer high hydraulic permeability to the soil, as long as the presence of clay and silt can confer low permeability and high-capacity water retention. Hence, the superficial hydrographic setting is highly influenced both by lithological outcrop units (clay–sand sediments) and by local morphology (different terrain slopes) [51]. Taking into account the soil map of Calabria (scale 1:250,000), in the study area, soil region corresponds to unit 62.3 (Hills of Calabria and Sicily on Tertiary calcareous rocks and sediments), which includes alluvial and coastal plains. The area of interest pertains to Soil Subregion 8, associated with the hilly background of the Tyrrhenian slope, where moderately steep to steep slopes (6–35%) occur at elevations below 300 MASL. This last soil subregion concerns the following soil system units: (i) slopes with different acclivity/substrate cropping zones, (ii) old terraces, and (iii) recent alluvial/colluvial deposits. In detail, according to the Soil Map of Calabria—1:250,000 scale, the pedological soil sub-systems that characterize the study area are represented in Figure 1. So, in the soil sub-system, units 6.3 and 6.6 occur in the study area, which correlate with landscapes with hummocky hill morphology with Pliocene pelitic/silty-pelitic sediments and complex slopes characterized by landslide phenomena with substrate consisting of chaotic Miocene pelites, respectively. The parent materials are mostly constituted of Mio-Pliocene and Quaternary sediments, on which the overlying soils exhibit the lack or occurrence of carbonates (pH: sub-acid to alkaline; texture: fine to coarse). In detail, the soil sub-system 6.3 is composed of the following soil typological units (STUs):

VIA\_1: Ap-BCg-Cg, slight to moderately thick profile, no coarse fragments, fine texture, alkaline, calcareous, medium/high water capacity, and poor drainage (Haplic-Gleyic Regosols).

SAL\_1: Ap-Bw-BCg-Cg, moderately deep profile, no coarse fragments, fine texture, alkaline, calcareous, high water capacity, and moderate drainage (Haplic Calcaric Cambisols).

GUA\_1: Ap-Bk-Ckg, moderate to very deep profile, no coarse fragments, fine texture, alkaline, high presence of carbonates, elevate water capacity, normal drainage, and slight tendency to crack in dry seasons (Haplic Calcisols).

Regarding to the cartographic unit 6.6, the following STUs occur:

CAO\_1: A-BC-Cg, shallow profile, frequent coarse fragments, fine textures, medium to high alkalinity, moderately saline, low-water capacity, and poor drainage (Calcaric-Hyposodic Regosols).

## 2.2. Data Processing and Workflow

In this paper, basic instruments were used for the tSHA variability retrieval to assess low-cost and no-time-consuming analyses. In the selected areas, many soil variations corresponding to texture, chemicals, and geodiversity changes were investigated. According to the physicochemical contrasts, the correlation of data occurred through a multi-analytical approach, matching different information obtained by various instruments.

As described in the following workflow (Figure 2), field and aerial surveys were conducted to collect and elaborate soil samples and UAS-RGB images, respectively. After the photogrammetry data collection, the data frame was computed by means of Agisoft Metashape (Agisoft LLC, St. Petersburg, Russia, version 2.0.1) for orthophotos generation. Orthophotos allow us to analyze soil characteristics and superficial variability by using red, green, and blue spectral indices, which are useful to appreciate the topsoil variability. The data frame is managed and analyzed by algorithms integrated into Quantum GIS (QGIS, version 3.18.3) and ENVI (version 5.3.1). For the preprocessing steps, ENVI software was used to normalize the image through a relative correction method by means of the

flatfield correction tool, while QGIS was used for the data frame manipulation and geoprocessing. Moreover, statistical data were processed by R-programming code, wherein the “ggcorrplot” and “Performance Analytics” packages were utilized, available in the CRAN (Comprehensive R Archive Network) platform.

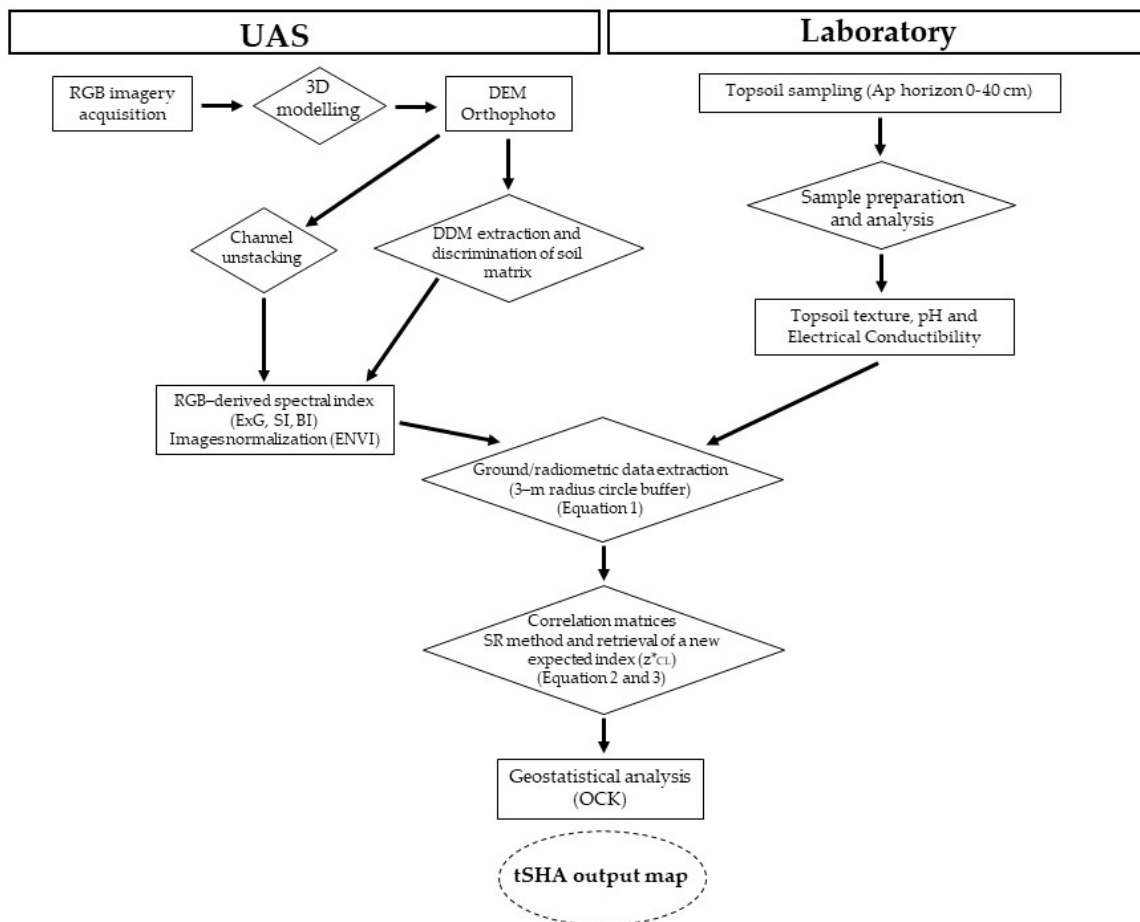


**Figure 2.** As part of the study of the tSHA distribution, the elaboration of the UAS-RGB image dataset started from image collection by UAS survey and topsoil ground data sampling. In the end, the final product (tSHA map) concerned data matching and the spatialization of laboratory and radiometric data.

Moreover, the combination of DEM is fundamental for the extraction of traits derived from the 3D model computations. According to this, by map algebra operations between DSM and DTM, it is possible to obtain results, such as DDMs from the difference between DSM and DTM. Hence, to isolate the soil matrix, DDM was converted into a vector file and then transformed into a mask, which was used for row subtraction on orthophotos. To ameliorate intra-row vegetation subtraction, the excess green (ExG) index was used.

Ground soil analysis, such as EC, pH, and textural classes, generally occur to support UAS data analysis [52,53]. In this study, such physicochemical parameters were performed in the laboratory through the appropriate methodologies, explained in detail in the following sections. According to this, linear regression models for each parameter were helpful to determine the most suitable analyte for the calibration of radiometric data. Hence, the best model was used for tSHA geostatistical spatial distribution, wherein the principal variable concerned the UAS-RGB radiometric data while the topographical layout was settled as the second variable.

### 2.3. Unmanned Aircraft System

UAS data were collected in August 2019 on two Greco Bianco (*Vitis vinifera* “Greco”) grapevine PUs. The horizontal and vertical flight accuracy corresponded to 0.5 m and 1.5 m,

respectively. Overflights were acquired through a DJI Phantom 4 Pro V2.04 tuned with an optical RGB camera (CMOS with 20 Megapixels of resolution, camera size:  $59 \times 41 \times 28$  mm and weight of 72 g) (Figure 3). Image acquisition was scheduled with an 80% image overlap ratio, a flying velocity of 5 m/s, and a 30 M.A.S.L., allowing a 10 cm pixel ground resolution for all surveys. The RGB camera includes blue (B), green (G), and red (R), which are part of the UAS acquisition system. Then, UAS-RGB images were processed to create 3D models and orthophotos. Indeed, based on structure from motion (SfM) algorithms, images were managed to create a 3D point cloud model of the study area [54]. Such techniques have gained great popularity due to the advent of several user-friendly software programs that allow for the management of spectral images datasets [55]. SfM works on the computer vision domain and enables 3D modeling and orthophotos production through the acquisition of a sequence of 2D overlapping images. SfM matches the same features in a compendium of overlapped images and computes, from diverse positions, camera orientation and positioning. As mentioned by Westoby et al. (2012) [55], this makes available the use of low-cost sensors and platforms for several applications. The photographic camera parameters are used to generate a densified point cloud model using multi-view stereo (MVS) algorithms [56]. The generation of orthophotos can be attained by applying specific processing steps to aerial surveys. In this research, the UAS-RGB dataset was used to generate specific maps related to soil salinity. So, through the common procedures for image alignment and feature matching, dense cloud point, mesh, and model texturization, it was possible to generate 3D models, digital elevation models (DEMs), and orthophoto maps.

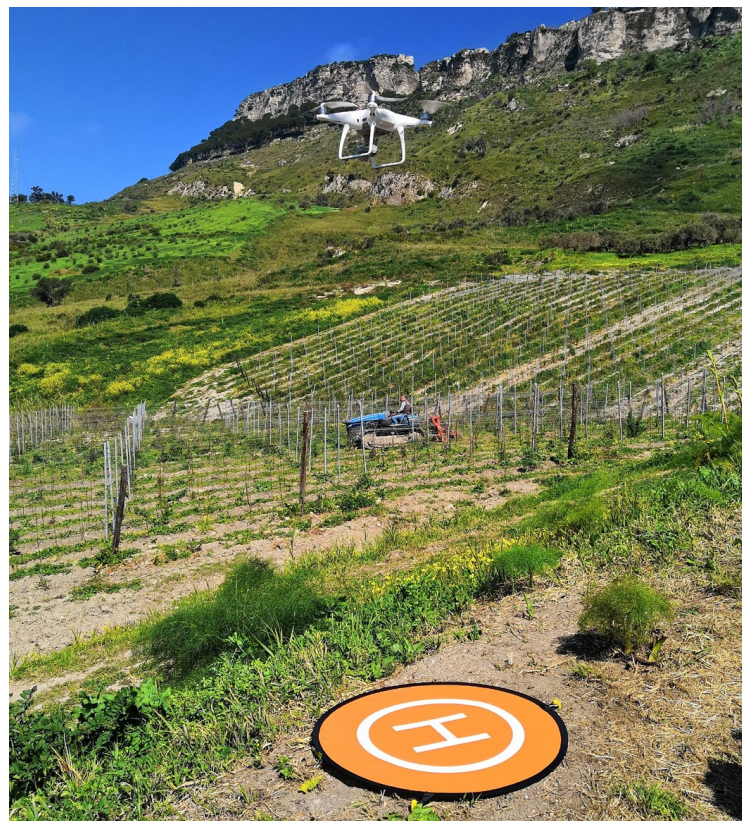


**Figure 3.** DJI Phantom 4 Pro V2.04 equipped with a 20 Mega-pixels resolution RGB camera.

#### 2.4. Physicochemical Analysis

Ground soil points were selected according to the radiometric and spectroradiometrical measurements acquired previously by Mei et al., 2020 [7]. Ground data were carried out during August 2019 (Figure 4) with bare soil evidence. Preparation and analysis were carried out at the CNR-IIA laboratories, investigating physicochemical parameters such as EC, pH, and topsoil texture. Soil samples were extracted in correspondence

with the pedological horizon Ap ( $\approx 0\text{--}40$  cm) and were prepared by drying at  $25^\circ\text{C}$  and by 2 mm sieve sifting. EC and pH were performed by the multiparameter instrument HANNA<sup>®</sup> HI9813-6, a portable measurer equipped with a unique probe that is in turn issued with the CAL Check HANNA<sup>®</sup> calibration functionality. The latter allows us to obtain more accurate measurements and report when the probe needs to be calibrated, cleaned, or replaced. For such analysis, mixtures of soil and purified water (MilliQ) were obtained, in a ratio of 1:2.5 by weight. Furthermore, to ensure the uniformity of sample solutions, a mechanical stirrer was used to obtain a homogeneous solution. Regarding the determination of topsoil texture, the field method involves an initial clod of soil of about 3/4 cm in diameter. Previously, the sample was moistened, successively held between the fingers, and manipulated. Such manipulation occurs following a guideline called "handling by touch", which can determine the soil texture, plasticity, and adhesiveness of the soil samples [5].

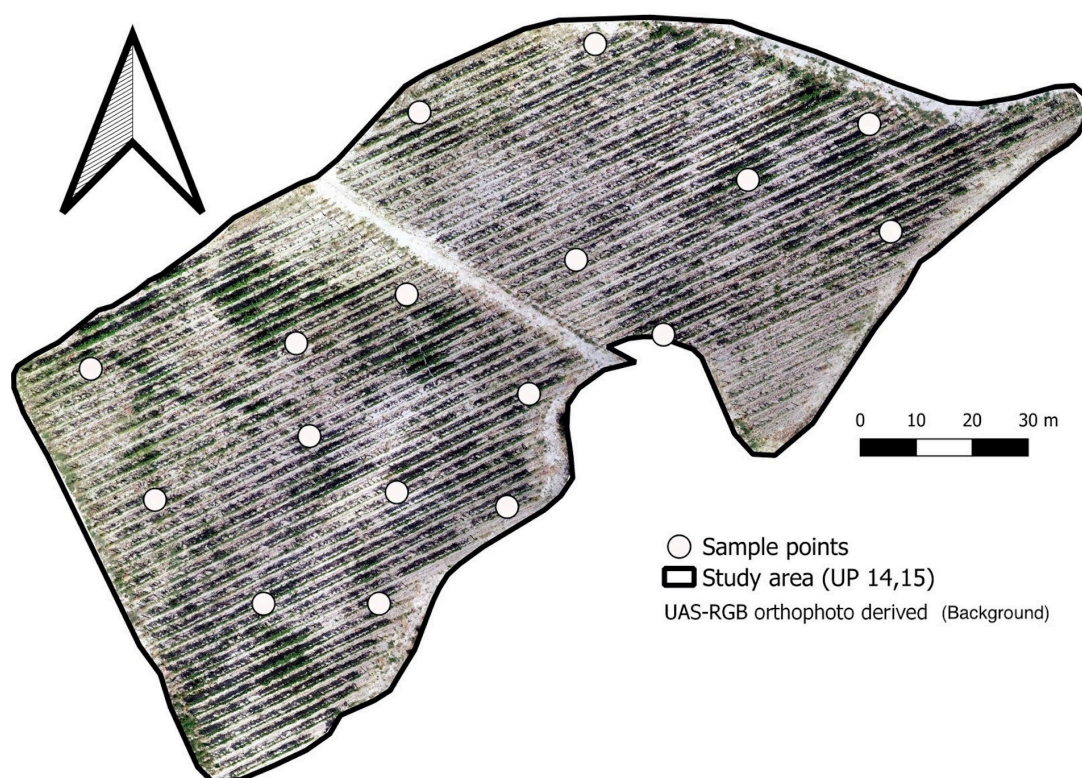


**Figure 4.** A UAS-derived product representing the spatial distribution of the samples into two PUs. In the background, a merged orthophoto of each PU and soil samples' spatial location.

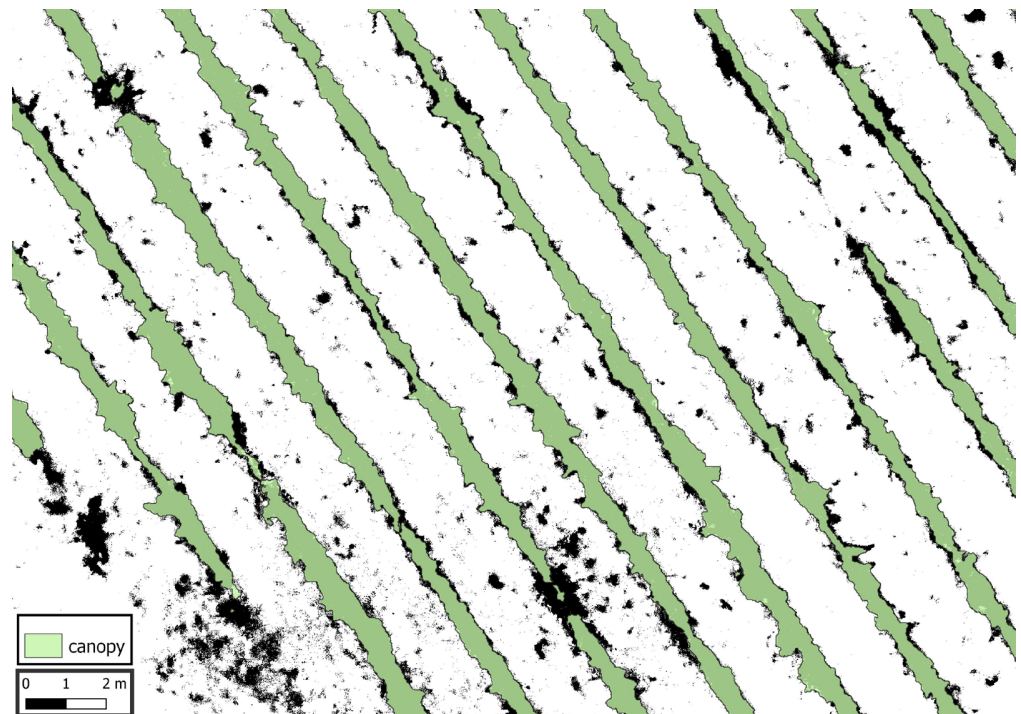
### 2.5. Remote Sensing Indices and Spectral Elaboration

A mathematical combination of spectral bands can provide an evaluation of several physicochemical properties of the soil. This information can be used to monitor vegetation, soil moisture, water quality, and other environmental parameters. In the RGB spectral range, there are several spectral indices that can be obtained to provide information about soil properties. Many studies have obtained information on land use and land use change, vegetation, and soil conditions [57,58]. Instead, the spectral indices were extracted, starting with an orthophoto representing two PUs. Spectral indices, based on RGB imagery (Table 1), concern the excess green (ExG), salinity index (SI), and brightness index (BI). The latter is fundamental in establishing a classification layer able to distinguish the vegetative contribution from the soil matrix and, furthermore, to detect the soil surface anomalies' distribution.

**Table 1.** Spectral indices used in this paper (blue band: B1; green band: B2; red band: B3).

Indices	Equation	Ref.
Excess green index (ExG)	$\text{ExG} = 2 \times \left( \frac{B2}{B3+B2+B1} \right) - \left( \frac{B3}{B3+B2+B1} \right) - \left( \frac{B1}{B3+B2+B1} \right)$	[59,60]
Salinity index (SI)	$\text{SI} = \sqrt{B2^2 \times B3^2}$	[22]
Brightness index (BI)	$\text{BI} = \sqrt{(B2^2 \times B3^2)/2}$	[26]

De facto, due to the high absorption in correspondence to the blue and red bands due to chlorophyll presence, the ExG index has been proven to be a useful tool for the discrimination of vegetational contribution [59,60]. The ExG index is calculated from the true color orthomosaic, using the raster calculator function on QGIS. The identification and separation of vegetation from soil, due to the development of the ExG index, is useful in terms of obtaining an exclusive soil radiometric discrimination closer to reality for each pixel. Consequently, a threshold layer is obtained from the ExG index, with the aim of isolating the soil matrix through binary values (0–1). Regarding the papers concerning the Otsu threshold value for vegetation classification [61,62], the soil's threshold layer is achieved by the raster calculation function, imposing values < 0.025 as characteristics of the soil matrix. In the end, the ExG raster is used as a threshold-based image classification to optimally distinguish vegetation from bare soil as a refinement of what was previously obtained by DDM acquisition (see Section 2.2). Hence, in the below picture (Figure 5), it is evident how the DDM's (green pattern) acquisition methodology combined with the ExG threshold-based (black pattern) raster image methodology had high efficiency in the subtraction of the vegetative contribution from soil pixels.

**Figure 5.** ExG threshold-based raster image (black) and DDM acquisition (green) for vegetation masking.

The correlation between radiometric (BI and SI) and physicochemical (soil texture, EC, pH) parameters is a key point for obtaining an accurate tSHA final map. Figure 6 shows a sampling grid with 3 m radius circle buffers used to extract radiometric data from



a soil image (without vegetation). Such a data frame (Equation (1)) is joined (by means of intersection and dissolving QGIS tools) with the laboratory data for statistical analysis.

$$z_{\mu}^*(x_0) = \mu_{ij}(x_n) \tag{1}$$

where  $z_{\mu}^*(x_0)$  represents the matrix resulting from the buffering operations in correspondence of the point  $x_0$ , comprehending the mean ( $\mu$ ) values to each  $j$ -indexed constraint EC ( $j = 1$ ), pH ( $j = 2$ ), clay content ( $j = 3$ ), and R/G/B bands ( $j = 4$ ) for each point ( $x_n$ ) and  $i$  statistical component.

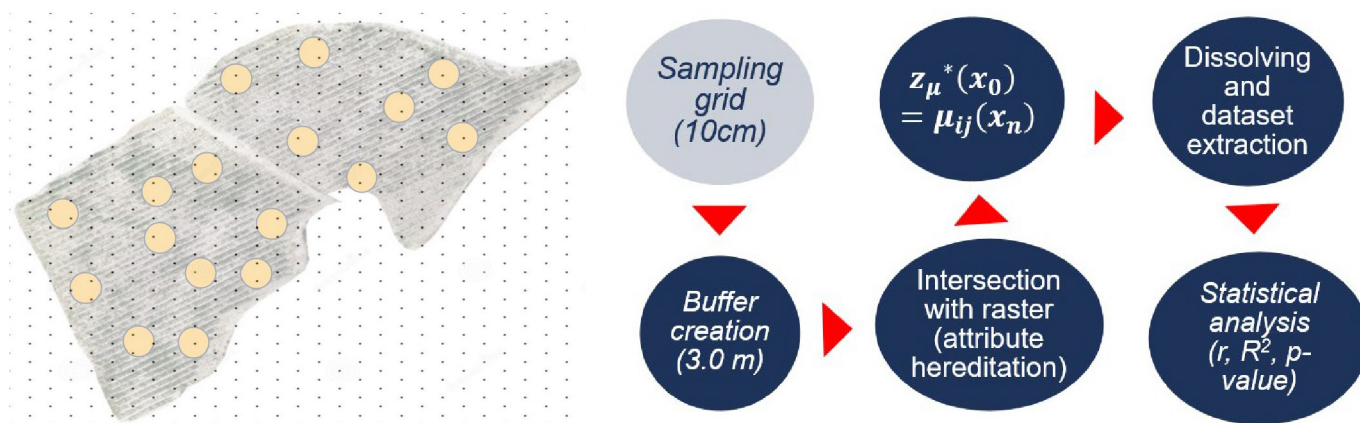


**Figure 6.** On the left, sampling grid and buffer creation (3 m radius) to extract pixel values from UAS and field topsoil data (not to scale). On the right, a smart workflow graphic (circular bending process), useful in showing the task’s steps regarding the radiometric and physicochemical data extraction processes.

Consequently, according to Douaoui et al., 2006 [22], a simple regression (SR) method is applied concerning the spectral index (SI and BI) more closely related to one of the ground topsoil parameters (texture, pH, and EC). The best parameters are obtained by statistical analysis and correlation matrices. The SR method is employed (Equation (2)) to provide a new expected index value obtained from the ground topsoil and the spectral index correlation, both extracted from the corresponding pixel by using Equation (1).

$$z_{SR}^*(s_0) = f[RSIndex(s_0)] \tag{2}$$

where  $z_{SR}^*$  represents the simple regression value for the point ( $s_0$ ),  $f$  corresponds to the regression function, and  $RSIndex$  is the spectral index value for the point ( $s_0$ ).

Indeed, following a statistical approach (such as SR), a line of the best fit provides the expected value through the obtainment of a new calibrated index ( $z_{CL}^*$ ). So, the correlation analysis between soil texture and radiometric data is employed in this study (as seen in Section 2.2) to raise the accuracy of data attained by UAS technologies. Consequently, the correlation coefficient and statistical significance coefficient ( $p$ -value) are obtained. Then, by means of ST method, the result (Equation (2)) is represented by the new retrieved spectral index ( $z_{CL}^*$ ). Through Equation (3), a novel spectral index ( $z_{CL}^*$ ) is achieved through the calibration operation among radiometric and physicochemical data.

$$z_{CL}^*(s_0) = 0.001ST + 0.069 \tag{3}$$

where  $z_{CL}^*$  is the new calibrated index, based on the previous SR approach, and  $ST$  is the soil texture parameter, selected to calibrate the new index by the good results obtained from the correlation matrices shown in Figures 7 and 8.

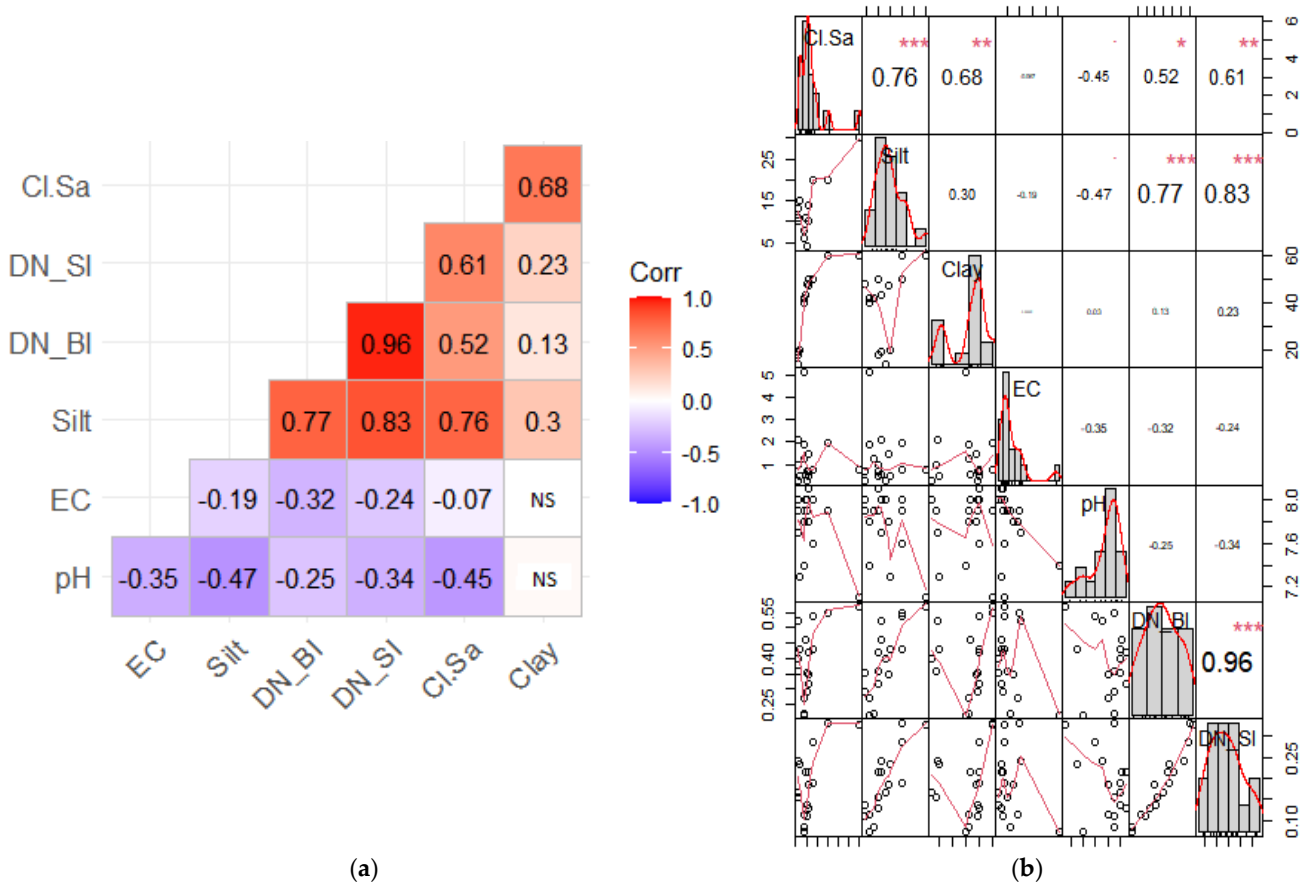


**Figure 7.** (a) Correlation matrix by using the package ggcorrplot. The parameters considered in this data frame are the following: clay, silt, sand, EC, pH, BI, and SI. (b) Visualization of a correlation matrix using the package PerformanceAnalytics. The parameters considered in this data frame are the following: clay, silt, sand, EC, pH, BI, and SI (diagonally: distribution of each variable). Instead, on the left side of the diagonal line, with a fitted line, the bivariate scatter plots are shown. On the right part of the diagonal line, the value of the correlation and the significance level are displayed as stars, wherein each significance level is related to one symbol:  $p$ -values (0, 0.001, 0.01, 0.05, 0.1) = symbols (\*\*\*, \*\*, \*, “blank”).

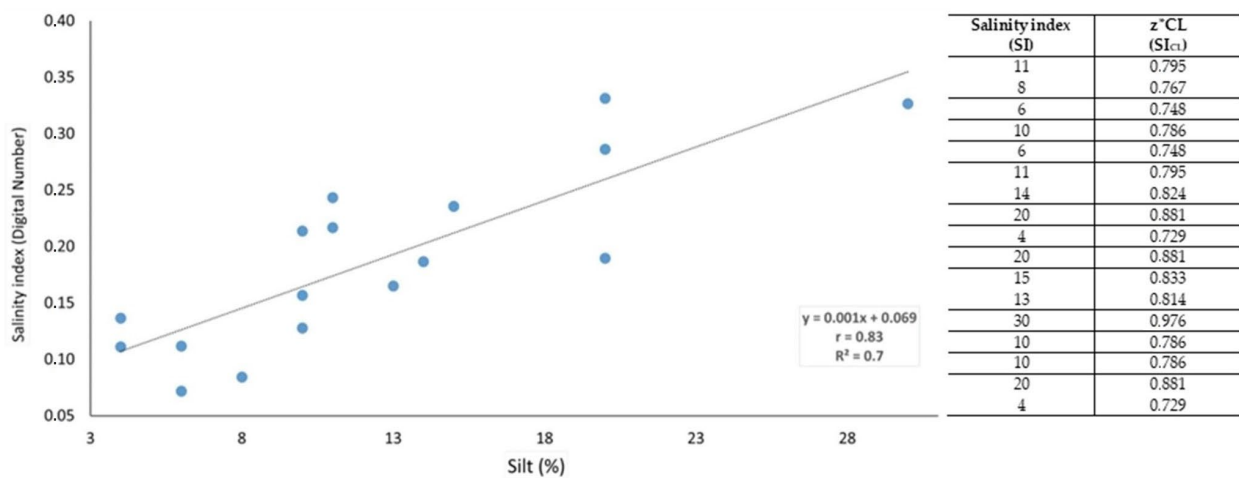


**Figure 8.** On the left, graphical visualization of the linear correlation between silt and salinity index (SI) and statistical information of the line equation, such as the Pearson and  $R^2$  coefficients. On the right, table representation of the dataset obtained from the calibration of spectral data through the line equation ( $y = 0.001x + 0.069$ ), obtained following the SR method (Equation (2)) applied to the silt and SI spectral index.

## 2.6. Geostatistical Analysis

Validation radiometric and soil ground data are elaborated through the ordinary cokriging (OCK) method, which calculates parameters through statistical simulations. Hence, this work used the  $z_{CL}^*$  index as a target variable (obtained from calibration of UAS and ground data) and DTM values as an auxiliary variable for the geostatistical interpolation. The OCK method was used due to the presence of an auxiliary variable as topography (extracted from DTM), measured at the same point as the target [63–73]. The OCK method is a variation of the ordinary kriging, adopted when relationships between the spatial distributions of various known parameters occur. This methodology outfits the determination of an empirical semivariogram, correlated with the spatial relationships and dependencies among data autocorrelation and cross-correlation. Then, in relation to the degree of spatial dependence of variables as a half-averaged squared difference between two known points, a semivariogram is modeled. Therefore, the OCK model involves the removal of each sample point from the dataset and the re-estimation of the values. The OCK map and semivariogram were performed using the R software and their `gstat` geostatistical, `sp` statistical, and `lattice` graphic packages. According to this, the R and QGIS environments were useful for statistical data manipulation, computing, and visualization. Being that the co-variable (DTM) is more densely sampled than the target variable ( $z_{CL}^*$ ), both variables were sampled uniformly in the QGIS environment by using buffering (3 m circle buffer, as performed above for spectral indices' extraction), intersection, and raster sample value algorithms. Consequently, the evaluation of kriging interpolation is shown by statistical accuracy measurements from the sample data set.

## 2.7. Validation

Validation process methodologies are used to indicate the quality of data obtained through statistical stochastic and deterministic approaches. Indeed, validation occurs to confirm the procedures employed for certain tests with the aim of judging the precision, accuracy, representativity, and significance of the results [74]. Due to several factors, such as the different density and distribution of samples along the study area, the performance of spatial interpolations needs to be evaluated with the aim of ensuring the reliability, precision, and accuracy of results [75]. The cross-validation (CV) method is a statistical approach that concerns the sequential omission of each measure to predict the value through the utilization of the rest of the dataset. Hence, error values are used to evaluate the accuracy of the model thanks to the comparison of statistical data, where  $p_i$  is the predicted value and  $m_i$  is the measured value at position “ $i$ ”. The root mean square error (RMSE), indicated below, is used as an indicator of accuracy and is regarded as the result of squaring the errors under the square root. It is considered the root mean square error that could be made during the model's construction. One of its advantages is that it concerns the same unit as the starting value, where overestimation reflects positive bias values and underestimation considers negative bias values.

$$RMSE = \sqrt{\frac{1}{n} \sum_{i=1}^n (p_i - m_i)^2}$$

The Pearson coefficient ( $r$ ) and its squared named coefficient of determination ( $R^2$ ) are often utilized to determine the performance of the spatial interpolation method. Both coefficients, shown in the next equations, lie in the range of  $-1$  to  $+1$ .

$$r = \frac{\sigma_{mp}}{\sigma_m \sigma_p}$$

$$R^2 = (r)^2$$

where  $\sigma_{mp}$  indicates the covariance between the two variables and  $\sigma_m\sigma_p$  is the product of these latter two variables.

### 3. Results

#### 3.1. Summary Statistics

In this paper, prediction maps came about from the spatial correlation of the soil texture and variables such as EC, pH, and spectral indexes. Therefore, regarding Equation (1), an interpolation of the nearest pixels via 3 m radius circle buffer allowed us to obtain the dataset shown in Table 2. Starting from ground sampling products, EC concentration ranged from 0.26 to 5.15 mS/cm, showing a mean value of around 1.20 and a median value of around 0.74. Instead, pH values varied from 7.1 to 8.1, with a mean value around 7.8 and a median value around 7.90. Furthermore, clay content reached percentage values from 14 to 60, showing a mean value of around 41 and a median value of around 47. The latter data and their statistical indicators, such as the mean, median, minimum value, maximum value, first quartile, third quartile, and deviation standard, are shown below in Table 2.

**Table 2.** This table represents the statistical summaries of the following parameters: Cl/Sa, silt, clay, EC, pH, BI (normalized), and SI (normalized). According to Equation (1), the nearest pixel interpolation through a 3 m radius circle buffer occurred, obtaining the following matrix of data. For each parameter, statistical indexes such as the mean, median, minimum value, maximum value, first quartile, third quartile, and deviation standard are also shown.

ID	CL/SA <sup>1</sup>	SILT	CLAY	EC	pH	BI_norm <sup>2</sup>	SI_norm <sup>2</sup>
1	0.935	11	43	0.55	8.01	0.4614	0.2166
2	0.840	8	42	1.25	7.90	0.2169	0.0843
3	0.808	6	42	1.86	7.80	0.2682	0.1118
4	0.250	10	18	0.96	7.90	0.3600	0.1567
5	0.741	6	40	5.15	7.40	0.2157	0.0717
6	0.272	11	19	2.11	7.70	0.5202	0.2433
7	1.205	14	47	1.47	7.80	0.3472	0.1865
8	3.000	20	60	1.99	7.90	0.5495	0.3313
9	1.000	4	48	0.65	7.90	0.2923	0.1120
10	1.667	20	50	0.74	8.00	0.4292	0.1896
11	0.308	15	20	0.48	7.30	0.4291	0.2355
12	0.192	14	13	0.26	8.00	0.3996	0.1650
13	6.000	30	60	0.78	7.10	0.5694	0.3266
14	1.250	10	50	0.69	8.10	0.4198	0.2137
15	1.250	10	50	0.48	8.10	0.3191	0.1277
16	1.667	20	50	0.72	7.60	0.5388	0.2861
17	1.000	4	48	0.26	8.00	0.3522	0.1364
Min	0.1918	4	14	0.26	7.10	0.2157	0.0717
Max	6	30	60	5.15	8.10	0.5694	0.3313
Mean	1.316	12	41	1.20	7.80	0.3935	0.1879
Median	1	11	47	0.74	7.90	0.3996	0.1865
First Qu	0.7407	8	40	0.55	7.70	0.3191	0.1277
Third Qu	1.25	15	50	1.47	8	0.4614	0.2356
$\sigma$ <sup>3</sup>	1.344	6.7	14	1.14	0.3	0.1084	0.0767

<sup>1</sup> Clay/sand ratio; <sup>2</sup> radiometric data normalized through flatfield correction tool on ENVI; <sup>3</sup> standard deviation.

The best fitting between soil and radiometric data occurred from the assessment of descriptive and inferential statistic indexes as the linear correlation degree ( $r$ ) and the significance degree ( $p$ -value). Then, through the R-packages `ggcorrplot` and `PerformanceAnalytics`, two correlation matrix plots of the previous dataset were obtained. The resulting plots were a heatmap, with the color and size of the squares indicating the strength of the linear correlation degree between variables, as well as a correlation matrix showing the distribution of each parameter and statistical indices (Figure 7a,b). In this study case, it was noticeable that soil textural parameters were more relatable to the radiometric ones, showing correlation degree ( $r$ ) values around 0.6 for the Cl/Sa and values around 0.8 for the silt. Instead, regarding the sample' significance degree ( $p$ -value), a value  $<0.001$  was found for silt and radiometric data, while it was for Cl/Sa  $< 0.01$  (Figure 7b).

According to the previous statistical analysis, the SI spectral index, by means of Equation (3) (see Section 2.5), was calibrated with the topsoil texture (silt) parameter. Indeed, by using the SR method (Equation (2)), it was possible to gain a new spectral index obtained first by the derived function and secondly by the line of best fit that provides the  $z_{CL}^*$  expected index (Figure 8).

### 3.2. Salinity Map by Means of Ordinary Cokriging (OCK)

A salinity map was obtained by applying a geostatistical approach to identify the tSHAs' distribution along two PUs. De facto, this type of approach can allow the operators to better handle their agronomic procedures. For this purpose, two forms of open-source software were used: RStudio for the obtaining of graph and result design, and QGIS for the final map edition.

Before the map edition, the spatial analysis methodology concerned, firstly, a step for exploratory data analysis by using trend maps and summary statistics; secondly, the creation of an experimental semivariogram and model fitting; thirdly, cross-validation operations; and fourthly, kriging interpolation. So, exploratory analysis was applied to obtain good knowledge of the data distribution (Figure 9). Thus, to achieve a normal distribution of data, a  $\log_{10}$  transformation of the  $SI_{CL}$  spectral index data set occurred. Therein, a first graphical representation of the data was ensued through the continuous density function. According to this, the density curve and the  $SI_{CL}$  spectral index data appeared to have very close mean and median values and showed that many samples lay around  $-0.10$ . Furthermore, a normal QQ plot was used to find the type of distribution for the  $SI_{CL}$  spectral index. Indeed, from this scatter plot, the data appeared uniformly distributed, forming a roughly straight line and showing a skewness value around 0.5 (Figure 9). A bubble map is represented, displaying  $SI_{CL}$  data values within the spatial setting. Indeed, the bubble map is a useful tool for visualizing the spatial distribution of the target variable, suggesting that the  $SI_{CL}$  spectral index values were distributed from NE to SW, showing an increasing trend. In the end, regarding the exploratory analysis, a Voronoi map was represented, showing polygons around each sample point. This type of diagram consists of a cell's boundaries based on the distance to the points around it and the respective values filling each polygon with the Voronoi map. From this graphical output, it is evident how the distribution of  $SI_{CL}$  spectral index values followed a NE-SW trend, wherein the highest values characterized the left-lowest part of the study area (Figure 9).

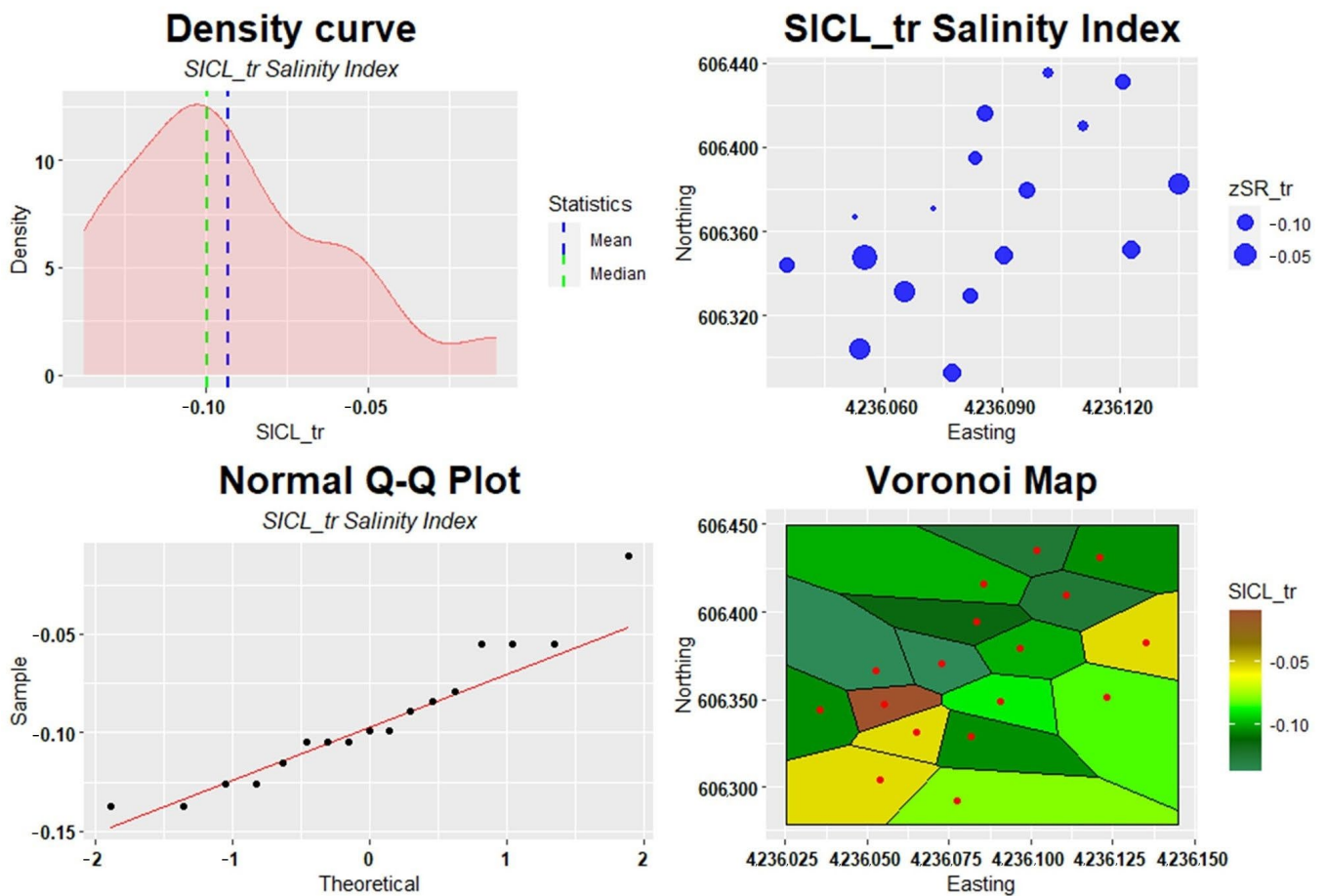


**Figure 9.** In the upper left part is a representation of the  $SI_{CL}$  ( $\log_{10}$  transformed) continuous density curve. In blue, the mean; in green, the median. In the upper right part, the  $SI_{CL}$  spectral index's bubble map is represented, characterized by an increasing trend of values from NE to SW. In the lower left part, there is a representation of the QQ plot that compares the ordered values of the  $SI_{CL}$  index with quantiles of the normal distribution. In the lower right part, a representation of the  $SI_{CL}$  spectral index's Voronoi map shows the highest values of concentration in the portion SW of the study area.

In Figure 10, the experimental OCK semivariogram is represented. The NE-SW search direction that constitutes the semivariogram concerns pairs of points falling within a sector defined by an aperture angle (tolerance) of  $\pm 22.5^\circ$ . The green arrow corresponds to the range (about 67 m), the orange arrow to the sill (1.0), and the yellow dot to the nugget (0.18). The semivariogram confirms a correlation between pairs of points ranging from 1 to 67 m (range on lag), while the semivariance suggests a nugget value around 0.18 and a sill value at 1 (normalized). Furthermore, as shown in Figure 11, there was a division of the area resulting from the relations between radiometric (UAS) and textural soil data (silt). So, the obtained spectral index  $SI_{CL}$  ( $z^*_{CL}$ ) confirmed patches with elevated estimates in the south-western study area section. Medium levels appeared within the middle part of the area as an N-S oriented configuration, whereas the lowest values lay in the east-northern portion of the study's parcel.

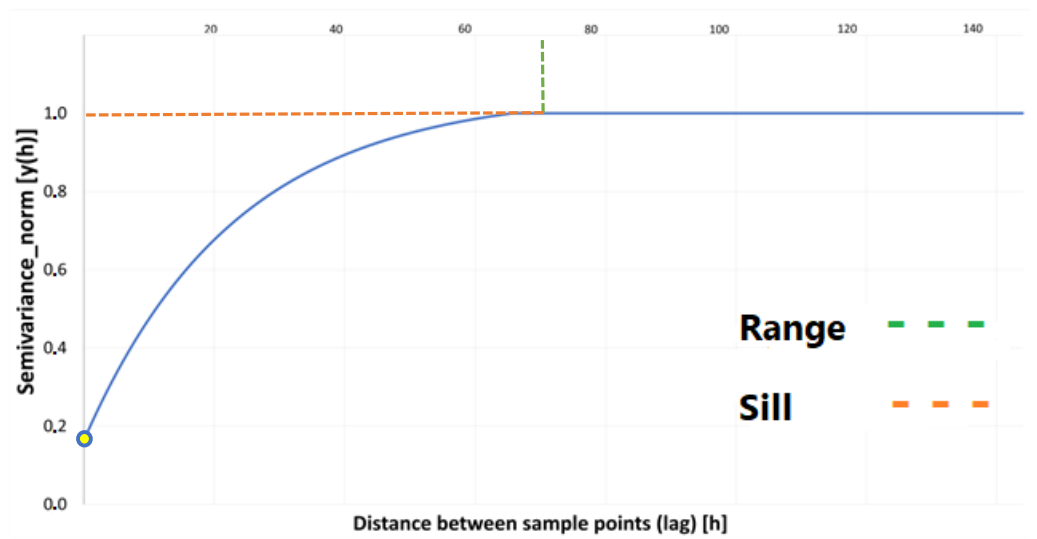


**Figure 10.** In blue, the OCK experimental semivariogram model. On the x-axis, distance is measured in meters. The angle corresponds to 22.5 degrees, including a north-east/south-west direction. The green line corresponds to the range (about 67 m), the orange line to the sill (1.0), and the yellow dot to the nugget (0.18).

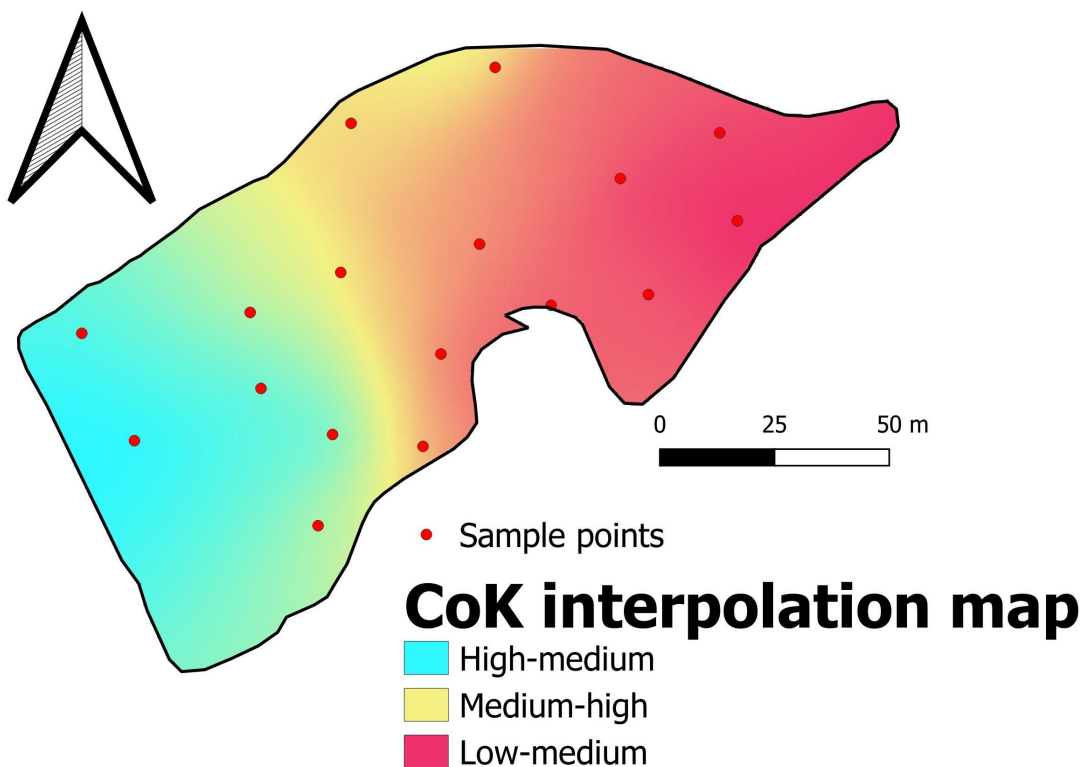


**Figure 11.** An OCK prediction salinity map signifying the spatialization between the spectral index  $SI_{CL}$  ( $z^*_{CL}$ ) as the target variable and topography values extracted from the DTM as the auxiliary variable. The land parcel subdivision in the three main tSHAs was evident, suggesting an increasing trend value of the  $SI_{CL}$  spectral index from NE to SW.

The  $SI_{CL}$  prediction map obtained through the OCK geostatistical method is reported by the summary descriptive statistics shown in Figure 12. In geostatistical analysis, it is fundamental to determine the measurement error in relation to the multiple measures per location. At locations where data were collected, the predicted values were not the same as

the measured values, differing from each other. According to this, MSE and RMSE values were determined, showing values around 0.398 and 0.013, respectively, and suggesting a moderate accuracy of the model (Figure 12).

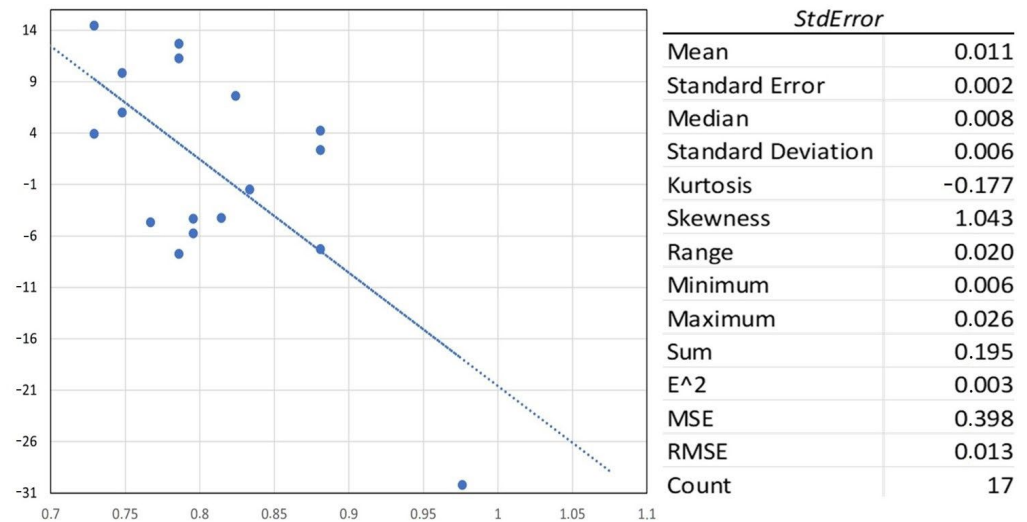


**Figure 12.** On the left, graphical representation of the OCK standard error plot. On the right, summary statistics of the standardized error (statistical validation), showing MSE and RMSE values around 0.398 and 0.013, respectively.

#### 4. Discussion

Farmers' needs are increasingly related to managing specific interventions over which to operate accurate agricultural practices (e.g., irrigation design, yield estimation). For instance, to optimize the management of land resources, agricultural operators need to manage water; tillage; and the usage of synthetic chemical fertilizers, herbicides, and other phytosanitary products [1,2,76]. According to this, many technologies can afford the knowledge of soil surface parameters' spatial distribution, where, albeit with less accuracy of results, the lowest time consumption and lowest cost instrumentation align with the usage of unmanned aircraft systems (UASs) and very high resolution (VHR) satellite imagery [7,13,22,28–32,77].

In PA and pedological contexts, it is fundamental to separate PUs into homogeneous soil areas [4,5,7,13,22]. This paper points out a methodology useful for the discrimination of topsoil homogeneous areas (tSHAs) along land parcels. This work obtained a good understanding of how tSHAs are distributed along land parcels by using a statistical/geostatistical approach. Results were achieved using low-cost and low-logistic instrumentation such as a UAS-RGB camera and topsoil (0–40 cm) texture, pH, and EC ground analysis. According to this, further information can be retrieved by using different resolutions of remote sensing instrumentation, following a downscaling approach starting with satellite, UAS, and a weighted/piloted pedological sampling campaign.

Again, this research aims to show how a preliminary low-cost UAS-RGB survey can be helpful in soil analysis by determining tSHAs over which to operate specific agricultural practices (e.g., irrigation design, yield estimation). Most of the recent papers focus on the use of drones for canopy parameter retrieval [38,40,41]. Instead, this work suggests how UAS-RGB can be used to compute architecture metrics to remove vegetation contributions along the study areas, providing only information for the soil matrix. Such issues, presented in this paper, are innovative and can represent a good low-cost approach for farmers. In fact, in PA and food supply chain contexts, good use of large-scale management on targeted interventions can feed an important contribution in reducing costs, waste, soil amendments, and agrochemicals utilization [1,2,4].



According to the previous discussion, by using low-cost analysis, such as UAS-RGB, soil texture, pH, and EC measurements, it can be possible for agricultural operators to determine tSHAs distribution along land parcels. Similarly, to minimize as much as possible the use of costly (e.g., hyperspectral camera) and highly logistic instrumentation (e.g., electromagnetometer), this work provides opportunities for small farms by using tools that can facilitate the organization of agricultural practices. Furthermore, knowing the distribution of tSHAs along wide land parcels allows, for instance, for the reduction of the extraction of samples during a pedological survey, minimizing costs related to laboratory activities. According to this, statistics can allow us to collect, organize, and interpret data, as well as support policy decisions. Moreover, one of the branches of applied statistics is geostatistics, useful in spatializing data for agronomy, geology, pedology, climate research, and atmospheric science. Finally, the information retrieved from these methodologies can be used for a decision-making support system.

Regarding the results, the  $SI_{CL}$  ( $z^*_{CL}$ ) map retrieval from UAS-RGB and soil ground data, obtained through statistical and geostatistical analysis, allow us to identify the distribution of tSHA along the study area. Firstly, image processing occurs by using photogrammetry techniques to extrapolate information. According to this, by using map algebra operations, the following products are obtained: (i) digital difference models (DDMs) and (ii) vegetation threshold raster retrieved by spectral index information (excess green). In this case, the discrimination of the soil bare matrix from the surrounding contribution of vegetation results in the successful management of high-quality data concerning only the soil pixel matrix. Secondly, a good statistical correlation between UAS-RGB indices and soil texture parameters (clay/sand ratio and silt contents) was achieved. Indeed, BI and SI indices matched better with physical parameters (Cl/Sa and Silt) than chemical ones (EC and pH). So, by using the UAS-RGB camera, pH, EC, and soil texture, tSHA discrimination allowed us to obtain good results in a low-cost environment. Hence, pointing out a sustainable methodology in the PA background is one of the main aims of this research, pondering quantitative final geostatistical spatialization on topsoil parameters. As concerning this paper, tSHA distribution can be spatialized also through the knowledge of auxiliary variables such as topographic information, allowing us to understand soil parameters that can influence, compared to others, mostly the PA context. Finally, by using a geostatistical methodology, a final thematic map was provided concerning the new  $SI_{CL}$  (salinity index calibrated) response, showing three main tSHAs over which farmers and agronomists can dispose of PA practices with more ease.

Furthermore, results from this research could be helpful for managing estimates of environmental parameters related to emissions of greenhouse gases (GHGs) and pollutants resulting from agricultural practices. Hence, 2018's world total GHGs emissions, due to agriculture and related land use/land use change, amounted to around 9.3 billion tons of carbon dioxide equivalent (Gt CO<sub>2</sub>eq). According to this, a rise of anthropogenic GHGs (e.g., CH<sub>4</sub>, NO<sub>x</sub>, CO<sub>2</sub>) emissions is expected due to the difficulties in agriculture management systems [78]. So, good management practices in agronomic policy can reduce a negative impact on the environment, helping to quantify parameters regarding air and soil pollutants [79,80].

Future research may point toward the preliminary detection of soil physicochemical variability distribution through the combination of technologies such as ground data (topsoil/subsoil), UAS (e.g., multispectral imagery), and VHR satellite imagery, considering other parameters such as soil organic matter (SOM), nutrient contents, available water capacity, pollutant/pesticide presence, or compaction degree.

## 5. Conclusions

This study deals with topsoil heterogeneity mapping in a precision agriculture (PA) context, based on ground data and UAS-RGB data. The results of this paper reinforce that different approaches, such as UAS and ground data, can be effective for the identification of topsoil homogeneous areas (tSHAs) in a determined pedo-climate context. Thus, the

UAS-RGB pixel matrix was calibrated with the physicochemical laboratory data. Therefore, through data correlation and calibration operations, a more precise salinity index ( $z^*_{CL}$ ) was obtained.

Furthermore, good UAS-RGB data handling appeared to be fundamental in the way of piloting future site-specific pedological sampling campaigns. Accordingly, a preliminary analysis along land parcels was found to be fundamental both for the detection of tSHA variability and soil typological unit (STU) mapping [5,7,13–17]. This study highlighted that salinity index (SI) and topsoil texture (silt content) may be adopted to improve the saline zones' detection along PUs, since they have the most reliable coefficient of correlation ( $R^2 = 0.70$ ). Thus, the calibration model and geostatistical spatialization (ordinary cokriging) of the salinity index resulted in being useful for the PUs' categorization into homogenous areas (e.g., tSHAs) where agricultural practice can be better administered. So, it was concluded that UAS-RGB data can support an extent of spatial topsoil recognition along land lots, aiming to constitute a dataset, for instance, of soil salinity distribution, helpful for pedologists, agronomists, and farmers.

In conclusion, three main tSHAs were identified, suggesting a variation in salinity content from low–medium to high–medium values. According to this, the improvement of the knowledge of topsoil parameters can occur through spatial heterogeneity detection along two PUs. Some positive effects retrieved from this work are the following: (i) planning agricultural practices in a PA context; (ii) substitution of proximal sensing techniques (high cost and heavy logistics) with low-cost and light logistic instrumentation (e.g., UAS-RGB); and (iii) advancements on site-specific crop management (SSCM) policies and local-based decision support systems (DSSs).

**Author Contributions:** Conceptualization, A.M. and A.V.R.; methodology, A.V.R., A.M., E.R. and G.F.; software, G.F., A.M. and A.V.R.; validation, A.V.R. and A.M.; formal analysis, A.V.R. and A.M.; data curation, A.M., G.F., E.R. and A.V.R.; writing—review and editing, A.M. and A.V.R.; supervision, A.M. All authors have read and agreed to the published version of the manuscript.

**Funding:** This work was carried out as part of the AMPA Project (Analisi Multi Parametrica per l'ambiente e l'Agricoltura)—POR Calabria FESR-FSE 2014–2020 (Project number: J68C17000090006).

**Data Availability Statement:** The data presented in this study are available on request from the corresponding author. The data are not publicly available due to the presence of data belonging to private agricultural companies.

**Conflicts of Interest:** The authors declare no conflict of interest.

## References

1. World Resources Institute. *1998–99 World Resources—A Guide to the Global Environment*; Oxford University Press: New York, NY, USA, 1998.
2. Crookston, K. A top 10 list of developments and issues impacting crop management and ecology during the past 50 years. *Crop Sci.* **2006**, *46*, 2253–2262. [[CrossRef](#)]
3. Mamo, M.; Malzer, G.L.; Mulla, D.J.; Huggins, D.J.; Strock, J. Spatial and temporal variation in economically optimum N rate for corn. *Agron. J.* **2003**, *95*, 958–964. [[CrossRef](#)]
4. Larson, W.E.; Robert, P.C. Farming by soil. In *Soil Management for Sustainability*; Lal, R., Pierce, F.J., Eds.; Soil and Water Conservation Society: Ankeny, IA, USA, 1991; pp. 103–112.
5. Costantini, E.A.C. *Linee Guida dei Metodi di Rilevamento e Informatizzazione dei Dati Pedologici*; Costantini, E.A.C., Ed.; CRA-ABP: Firenze, Italy, 2007; p. 280.
6. Corwin, D.L.; Lesch, S.M. Apparent soil electrical conductivity measurements in agriculture. *Comput. Electron. Agric.* **2005**, *46*, 11–43. [[CrossRef](#)]
7. Mei, A.; Fontinovo, G.; Rantica, E.; Allegrini, A. Integration of satellite, UAV and field data for soil analysis in precision viticulture. *Rend. Online Soc. Geol. It.* **2020**, *52*, 33–39. [[CrossRef](#)]
8. Lamb, D.; Hall, A.; Louis, J. Airborne remote sensing of vines for canopy variability and productivity. *Aust. Grapegrow. Winemak.* **2001**, 89–94.
9. Colombo, C.; Miano, T. *Metodi di Analisi Chimica Del Suolo*; Società Italiana della Scienza del Suolo, Associazione Italiana dei Laboratori Pubblici di Agrochimica, Ed.; Pubblicità e Stampa: Modugno, Italy, 2015.
10. Benedetti, F.; Caon, L. *Global Soil Laboratory Assessment 2020—Laboratories' Capacities and Needs*; FAO: Rome, Italy, 2021.

11. Adamchuk, V.I.; Hummel, J.W.; Morgan, M.T.; Upadhyaya, S.K. On-the-go soil sensors for precision agriculture. *Comput. Electron. Agric.* **2004**, *44*, 71–91. [[CrossRef](#)]
12. Viscarra Rossel, R.A.; Walvoort, D.J.J.; McBratney, A.B.; Janik, L.J.; Skjemstad, J.O. Visible, near infrared, mid infrared or combined diffuse reflectance spectroscopy for simultaneous assessment of various soil properties. *Geoderma* **2006**, *131*, 59–75. [[CrossRef](#)]
13. Barbetti, R. Low-cost digital mapping of soil organic carbon using optical spectrophotometer and Sentinel-2 image. *EQA Int. J. Environ. Qual.* **2021**, *44*, 1–8. [[CrossRef](#)]
14. Pichon, L.; Leroux, C.; Macombe, C.; Taylor, J.; Tisseyre, B. What relevant information can be identified by experts on unmanned aerial vehicles' visible images for precision viticulture. *Precis. Agric.* **2019**, *20*, 278–294. [[CrossRef](#)]
15. Cillero Castro, C.; Domínguez Gómez, J.A.; Delgado Martín, J.; Hinojo Sánchez, B.A.; Cereijo Arango, J.L.; Cheda Tuya, F.A.; Díaz-Varela, R. An UAV and Satellite Multispectral Data Approach to Monitor Water Quality in Small Reservoirs. *Remote Sens.* **2020**, *12*, 1514. [[CrossRef](#)]
16. Matese, A.; Toscano, P.; Di Gennaro, S.; Genesio, L.; Vaccari, F.; Primicerio, J.; Claudio, B.; Zaldei, A.; Bianconi, R.; Gioli, B. Intercomparison of UAV, Aircraft and Satellite Remote Sensing Platforms for Precision Viticulture. *Remote Sens.* **2015**, *7*, 2971–2990. [[CrossRef](#)]
17. Hu, J.; Peng, J.; Zhou, Y.; Xu, D.; Zhao, R.; Jiang, Q.; Fu, T.; Wang, F.; Shi, Z. Quantitative Estimation of Soil Salinity Using UAV-Borne Hyperspectral and Satellite Multispectral Images. *Remote Sens.* **2019**, *11*, 736. [[CrossRef](#)]
18. Turner, N.; Colmer, T.; Quealy, J.; Pushpavalli, R.; Krishnamurthy, L.; Kaur, J.; Singh, G.; Siddique, K.; Vadez, V. Salinity tolerance and ion accumulation in chickpea (*Cicer arietinum* L.) subjected to salt stress. *Plant Soil* **2013**, *365*, 347–361. [[CrossRef](#)]
19. Eltner, A.; Schneider, D. Analysis of Different Methods for 3D Reconstruction of Natural Surfaces from Parallel-Axes UAV Images. *Photogram Rec.* **2015**, *30*, 279–299. [[CrossRef](#)]
20. Khan, S.A.; Mulvaney, R.L.; Hoef, R.G. A Simple Soil Test for Detecting Sites that are Nonresponsive to Nitrogen Fertilization. *Soil Sci. Soc. Am. J.* **2001**, *65*, 1751–1760. [[CrossRef](#)]
21. Khan, N.; Rastokuev, V.; Sato, Y.; Shiozawa, S. Assessment of hydrosaline land degradation by using a simple approach of remote sensing indicators. *Agric. Water Manag.* **2005**, *77*, 96–109. [[CrossRef](#)]
22. Abdelkader, D.; Nicolas, H.; Walter, C. Detecting salinity hazards within a semiarid context by means of combining soil and remote-sensing data. *Geoderma* **2006**, *134*, 217–230. [[CrossRef](#)]
23. Castaldi, F.; Casa, R.; Castrignanò, A.; Pascucci, S.; Palombo, A.; Pignatti, S. Estimation of soil properties at the field scale from satellite data: A comparison between spatial and non-spatial techniques. *Eur. J. Soil. Sci.* **2014**, *65*, 842–851. [[CrossRef](#)]
24. Castaldi, F.; Palombo, A.; Santini, F.; Pascucci, S.; Pignatti, S.; Casa, R. Evaluation of the potential of the current and forthcoming multispectral and hyperspectral imagers to estimate soil texture and organic carbon. *Remote Sens. Environ.* **2016**, *179*, 54–65. [[CrossRef](#)]
25. Novak, J.; Lukas, V.; Kren, J. Estimation of soil properties based on soil colour index. *Agric. Conspec. Sci.* **2018**, *83*, 71–76.
26. Escadafal, R. Remote sensing of arid soil surface color with Landsat thematic mapper. *Adv. Space Res.* **1989**, *9*, 159–163. [[CrossRef](#)]
27. Ubina, N.A.; Cheng, S.-C. A Review of Unmanned System Technologies with Its Application to Aquaculture Farm Monitoring and Management. *Drones* **2022**, *6*, 12. [[CrossRef](#)]
28. Nouri, H.; Chavoshi Borujeni, S.; Alaghmand, S.; Anderson, S.J.; Sutton, P.C.; Parvazian, S.; Beecham, S. Soil Salinity Mapping of Urban Greenery Using Remote Sensing and Proximal Sensing Techniques; The Case of Veale Gardens within the Adelaide Parklands. *Sustainability* **2018**, *10*, 2826. [[CrossRef](#)]
29. Kim, J.; Kim, S.; Ju, C.; Son, H.I. Unmanned aerial vehicles in agriculture: A review of perspective of platform, control, and applications. *IEEE Access* **2019**, *7*, 105100–105115. [[CrossRef](#)]
30. Radoglou-Grammatikis, P.; Sarigiannidis, P.; Lagkas, T.; Moscholios, I. A compilation of UAV applications for precision agriculture. *Comput. Netw.* **2020**, *172*, 107148. [[CrossRef](#)]
31. Liu, X.; Chen, S.W.; Nardari, G.V.; Qu, C.; Ojeda, F.C.; Taylor, C.J.; Kumar, V. Challenges and Opportunities for Autonomous Micro-UAVs in Precision Agriculture. *IEEE Micro* **2022**, *42*, 61–68. [[CrossRef](#)]
32. Singh, A.P.; Yerudkar, A.; Mariani, V.; Iannelli, L.; Glielmo, L. A Bibliometric Review of the Use of Unmanned Aerial Vehicles in Precision Agriculture and Precision Viticulture for Sensing Applications. *Remote Sens.* **2022**, *14*, 1604. [[CrossRef](#)]
33. Torres-Sánchez, J.; Peña, J.M.; De Castro, A.I.; López-Granados, F. Multi-temporal mapping of the vegetation fraction in early season wheat fields using images from UAV. *Comput. Electron. Agric.* **2014**, *103*, 104–113. [[CrossRef](#)]
34. Spetsakis, M.E.; Aloimonos, Y. A multi-frame approach to visual motion perception. *Int. J. Comput. Vis.* **1991**, *6*, 245–255. [[CrossRef](#)]
35. Boufama, B.; Mohr, R.; Veillon, F. Euclidean Constraints on Uncalibrated Reconstruction. In Proceedings of the Fourth International Conference on Computer Vision, Berlin, Germany, 11–14 May 1993; pp. 466–470.
36. Szeliski, R.; Kang, S.B. Recovering 3-D shape and motion from image streams using nonlinear least squares. *J. Vis. Commun. Image Represent.* **1994**, *5*, 10–28. [[CrossRef](#)]
37. Förstner, W. A feature-based correspondence algorithm for image matching. *Int. Arch. Photogramm. Remote Sens.* **1986**, *26*, 150–166.
38. Haboudane, D.; Miller, J.R.; Tremblay, N.; Zarco-Tejada, P.J.; Dextraze, L. Integrated narrow-band vegetation indices for prediction of crop chlorophyll content for application to precision agriculture. *Remote Sens. Environ.* **2002**, *81*, 416–426. [[CrossRef](#)]
39. Dadshani, S.; Kurakin, A.; Amanov, S. Non-invasive assessment of leaf water status using a dual mode microwave resonator. *Plant Methods* **2015**, *11*, 8. [[CrossRef](#)]

40. Orlando, F.; Movedi, E.; Coduto, D.; Parisi, S.; Brancadoro, L.; Pagani, V.; Guarneri, T.; Confalonieri, R. Estimating leaf area index (LAI) in vineyards using the Pocket LAI smart-app. *Sensors* **2016**, *16*, 2004. [[CrossRef](#)]
41. Hubbard, S.S.; Schmutz, M.; Balde, A.; Falco, N.; Peruzzo, L.; Dafflon, B.; Leger, E.; Wu, Y. Estimation of soil classes and their relationship to grapevine vigor in a Bordeaux vineyard: Advancing the practical joint use of electromagnetic induction (EMI) and NDVI datasets for precision viticulture. *Precis. Agric.* **2021**, *22*, 1353–1376. [[CrossRef](#)]
42. Pichon, L.; Ducanhez, A.; Fonta, H.; Tisseyre, B. Quality of Digital Elevation Models Obtained from Unmanned Aerial Vehicles for Precision Viticulture. *OENO One* **2016**, *50*. [[CrossRef](#)]
43. Williams, R.D. DEMs of difference. *Geomorphol. Tech.* **2012**, *2*, 1–12.
44. Köppen, W. *Das Geographische System der Klimate*, 1–44; Gebrüder Borntraeger: Berlin, Germany, 1936.
45. Critelli, S. The interplay of lithospheric flexure and thrust accommodation in forming stratigraphic sequences in the southern Apennines foreland basin system, Italy. *Rend. Lincei* **1999**, *10*, 257–326. [[CrossRef](#)]
46. Perri, F.; Cirrincione, R.; Critelli, S.; Mazzoleni, P.; Pappalardo, A. Clay Mineral Assemblages and Sandstone Compositions of the Mesozoic Longobucco Group, Northeastern Calabria: Implications for Burial History and Diagenetic Evolution. *Int. Geol. Rev.* **2008**, *50*, 1116–1131. [[CrossRef](#)]
47. Malinverno, A.; Ryan, W.B. Extension in the Tyrrhenian Sea and shortening in the Apennines as result of arc migration driven by sinking of the lithosphere. *Tectonics* **1986**, *5*, 227–245. [[CrossRef](#)]
48. Servizio Geologico d'Italia. *Carta Geologica d'Italia alla Scala 1:50,000, F. 590 Taurianova*; ISPRA: Rome, Italy, 2015.
49. Cavazza, W.; Blenkinsop, J.; De Celles, P.G.; Patterson, R.T.; Reinhardt, E.G. Stratigrafia e sedimentologia della sequenza sedimentaria oligocenica-quadernaria del bacino Calabro Ionico. *Boll. Soc. Geol. Ital.* **1997**, *116*, 51–77.
50. Cavazza, W.; Ingersoll, R.V. Detrital Modes of the Ionian forearc basin fill (Oligocene–Quaternary) reflect the tectonic evolution of the Calabria–Peloritani terrane (Southern Italy). *J. Sediment. Res.* **2005**, *75*, 268–279. [[CrossRef](#)]
51. Servizio Agropedologico della Calabria. *Carta Dei Suoli a Scala 1:250,000*; ARSAC: Rome, Italy, 2003.
52. Fernandez-Buces, N.; Siebe, C.; Cram, S.; Palacio, J.L. Mapping soil salinity using a combined spectral response index for bare soil and vegetation: A case study in the former lake Texcoco, Mexico. *J. Arid. Environ.* **2006**, *65*, 644–667. [[CrossRef](#)]
53. Akramkhanov, A.; Vlek, P.L. The assessment of spatial distribution of soil salinity risk using neural network. *Environ. Monit. Assess.* **2012**, *184*, 2475–2485. [[CrossRef](#)]
54. Carrivick, J.; Smith, M.; Quincey, D. Structure from motion photogrammetry in physical geography. *Prog. Phys. Geogr.* **2016**, *40*, 247–275. [[CrossRef](#)]
55. Westoby, M.J.; Brasington, J.; Glasser, N.F.; Hambrey, M.J.; Reynolds, J.M. Structure-from-Motion' photogrammetry: A low-cost, effective tool for geoscience applications. *Geomorphology* **2012**, *179*, 300–314. [[CrossRef](#)]
56. Ahmadabadian, A.H.; Yazdan, R.; Karami, A.; Moradi, M.; Ghorbani, F. Clustering and selecting vantage images in a low-cost system for 3D reconstruction of texture-less objects. *Measurement* **2017**, *99*, 185–191. [[CrossRef](#)]
57. Rouse, J.W.; Haas, R.H.; Schell, J.A.; Deering, D.W. Monitoring vegetation system in the great plains with ERTS. In Proceedings of the Third Earth Resources Technology Satellite-1 Symposium, Greenbelt, MD, USA, 10–14 December 1973; pp. 3010–3017, NASA SP-351.
58. Khan, N.M.; Rastoskuev, V.V.; Shalina, E.V.; Sato, Y. Mapping Salt-Affected Soils Using Remote Sensing Indicators—A Simple Approach with the Use of GIS IDRISI. In Proceedings of the 22nd Asian Conference on Remote Sensing, Singapore, 5–9 November 2001; pp. 5–9.
59. Parker, T.A.; Palkovic, A.; Gepts, P. Determining the Genetic Control of Common Bean Early-Growth Rate Using Unmanned Aerial Vehicles. *Remote Sens.* **2020**, *12*, 1748. [[CrossRef](#)]
60. Wobbecke, D.M.; Meyer, G.E.; Von Barga, K.; Mortensen, D.A. Color indices for weed identification under various soil, residue, and lighting conditions. *Trans. ASAE* **1995**, *38*, 259–269. [[CrossRef](#)]
61. Otsu, N. A Threshold Selection Method from Gray-Level Histograms. *IEEE Trans. Syst. Man Cybern.* **1979**, *9*, 62–66. [[CrossRef](#)]
62. Kim, D.W.; Yun, H.S.; Jeong, S.J.; Kwon, Y.S.; Kim, S.G.; Lee, W.S.; Kim, H.J. Modeling and Testing of Growth Status for Chinese Cabbage and White Radish with UAV-Based RGB Imagery. *Remote Sens.* **2018**, *10*, 563. [[CrossRef](#)]
63. Matheron, G. Principles of Geostatistics. *Econ. Geol.* **1963**, *58*, 1246–1266. [[CrossRef](#)]
64. Myers, D.E. Matrix formulation of co-kriging. *Math. Geol.* **1982**, *14*, 249–257. [[CrossRef](#)]
65. Li, J.; Heap, A.D. A review of comparative studies of spatial interpolation methods in environmental sciences: Performance and impact factors. *Ecol. Inf.* **2011**, *6*, 228–241. [[CrossRef](#)]
66. Rivoirard, J. *Introduction to Disjunctive Kriging and Non-Linear Geostatistics*; Clarendon Press: Oxford, UK, 1994.
67. Chilès, J.-P.; Delfiner, P. *Chapter 4 of Geostatistics: Modeling Spatial Uncertainty*; John Wiley & Sons, Inc.: New York, NY, USA, 1999.
68. Cressie, N. *Statistics for Spatial Data*; Wiley: New York, NY, USA, 1993; p. 326.
69. Cressie, N.; Hawkins, D.M. Robust estimation of the variogram. *Math. Geol.* **1980**, *12*, 115–125. [[CrossRef](#)]
70. Krivoruchko, K. *Spatial Statistical Data Analysis for GIS Users*; Esri Press: Redlands, CA, USA, 2011; p. 928.
71. Laurent, L.; Boucard, P.; Soulier, B. Generation of a cokriging metamodel using a multiparametric strategy. *Comput. Mech.* **2013**, *51*, 151–169. [[CrossRef](#)]
72. Wackernagel, H. *Multivariate Geostatistics: An Introduction with Applications*; Springer-Verlag: Berlin, Germany, 1995.
73. Wang, K.; Zhang, C.; Li, W. Predictive mapping of soil total nitrogen at a regional scale: A comparison between geographically weighted regression and cokriging. *Appl. Geogr.* **2013**, *42*, 73–85. [[CrossRef](#)]

74. Stamatis, D.H. *Understanding ISO 9000 and Implementing the Basics to Quality*, 1st ed.; Routledge: New York, NY, USA, 1995.
75. Li, J.; Heap, A.D. *A Review of Spatial Interpolation Methods for Environmental Scientists*; Record 2008/23, 137; Geoscience Australia: Canberra, Australia, 2008.
76. FAO. Emissions Due to Agriculture. Global, Regional and Country Trends 2000–2018. FAOSTAT Analytical Brief Series No 18. Rome. 2020. Available online: <https://www.fao.org/3/cb3808en/cb3808en.pdf> (accessed on 8 June 2023).
77. Ragazzo, A.V.; Mei, A.; Fontinovo, G. Unmanned Aircraft Systems and Satellite Technologies for Topsoil Mapping in Precision Agriculture. *Int. Arch. Photogramm. Remote Sens. Spatial Inf. Sci.* **2023**, *48*, 417–422. [[CrossRef](#)]
78. Wato, T.; Amare, M. The agricultural water pollution and its minimization strategies—A review. *J. Resour. Dev. Manag.* **2020**, *64*, 10–22.
79. Tubiello, F.N.; Salvatore, M.; Rossi, S.; Ferrara, A.; Fitton, N.; Smith, P. The FAOSTAT database of greenhouse gas emissions from agriculture. *Environ. Res. Lett.* **2013**, *8*, 015009. [[CrossRef](#)]
80. Höglund-Isaksson, L.; Gómez-Sanabria, A.; Klimont, Z.; Rafaj, P.; Schöpp, W. Technical potentials and costs for reducing global anthropogenic methane emissions in the 20z50 timeframe—Results from the GAINS model. *Environ. Res. Commun.* **2020**, *2*, 025004. [[CrossRef](#)]

**Disclaimer/Publisher’s Note:** The statements, opinions and data contained in all publications are solely those of the individual author(s) and contributor(s) and not of MDPI and/or the editor(s). MDPI and/or the editor(s) disclaim responsibility for any injury to people or property resulting from any ideas, methods, instructions or products referred to in the content.